ACS central science

http://pubs.acs.org/journal/acscii

Research Article

Copper Organometallic Iodide Arrays for Efficient X-ray Imaging Scintillators

Hong Wang, Jian-Xin Wang, Xin Song, Tengyue He, Yang Zhou, Osama Shekhah, Luis Gutiérrez-Arzaluz, Mehmet Bayindir, Mohamed Eddaoudi, Osman M. Bakr, and Omar F. Mohammed*

Cite This: *ACS Cent. Sci.* 2023, 9, 668–674

Read Online

ACCESS | Metrics & More | Article Recommendations | Supporting Information

ABSTRACT: Lead-free organic metal halide scintillators with low-dimensional electronic structures have demonstrated great potential in X-ray detection and imaging due to their excellent optoelectronic properties. Herein, the zero-dimensional organic copper halide $(18\text{-crown-6})_2Na_2(H_2O)_3Cu_4I_6$ (CNCI) which exhibits negligible self-absorption and near-unity green-light emission was successfully deployed into X-ray imaging scintillators with outstanding X-ray sensitivity and imaging resolution. In particular, we fabricated a CNCI/polymer composite scintillator with an ultrahigh light yield of ∼109,000 photons/MeV, representing one of the highest values reported so far for scintillation materials. In addition, an ultralow detection limit of 59.4 nGy/s was achieved, which is approximately 92 times lower than the dosage for a standard medical examination. Moreover, the spatial imaging resolution of the CNCI scintillator was further improved by using a silicon template due to the wave-guiding of light through CNCI-filled pores. The pixelated CNCI-silicon array scintillation screen displays an impressive spatial resolution of 24.8 line pairs per millimeter (lp/mm) compared to the resolution of 16.3 lp/mm for CNCI-polymer film screens, representing the highest resolutions reported so far for organometallic-based X-ray imaging screens. This design represents a new approach to fabricating high-performance X-ray imaging scintillators based on organic metal halides for applications in medical radiography and security screening.

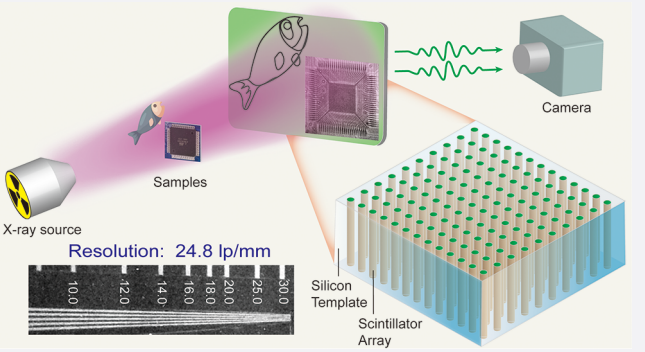

X-ray imaging scintillators have been extensively used in the fields of medical diagnosis, defense security, and nondestructive inspection.[1−6] In a typical X-ray scintillation process, X-ray absorption, photogeneration of charge carriers, and radiative carrier recombination are the key steps that lead to radioluminescence.[1] Therefore, a high-performance scintillator material needs to meet at least two basic requirements: strong X-ray absorption and high photoluminescence quantum yield (PLQY). To date, many all-inorganic lead halide perovskites materials, such as $CsPbX_3$ (X = I^-, Br^-, Cl^-, or mixed halides) and related low-dimensional structures, have been developed as high-performance scintillators due to their high X-ray absorption, low detection limit, and good spatial imaging resolution.[7−11] However, the toxicity of lead in these halide perovskites and the perovskites' notorious instability under humid conditions have greatly limited the materials' further development and commercialization.[12,13] Therefore, exploring lead-free materials with high stability, low toxicity, low cost, high X-ray absorption cross-section, and high light yield for high-performance X-ray imaging scintillators is urgently needed.

To address these shortcomings, various eco-friendly lead-free metal halide scintillators, such as $Cu(I)^-$, $Ag(I)^-$, $Mn(II)^-$, $Sb(III)^-$, and $Sn(IV)^-$ perovskite materials, have been fabricated.[14−22] In this context, low-dimensional all-inorganic copper halides have been extensively studied because of their multiple structural variations, high PLQY, and large Stokes shift. More importantly, the rapid development of all-inorganic copper halides for X-ray detection and imaging has led to extended research into their organic copper halide counterparts, which exhibit significantly improved environmental stability and distinct optoelectronic properties, such as more localized excited electronic states and stronger exciton−phonon coupling.[23−26]

Nevertheless, due to the strong light scattering at grain boundaries of copper halide/polymer composite scintillation

Received: December 16, 2022
Published: March 10, 2023

Scheme 1. Pixelated Screens Confine Scintillating Light in Silicon Pores through Total Internal Reflection and Enhance Imaging Resolution[a]

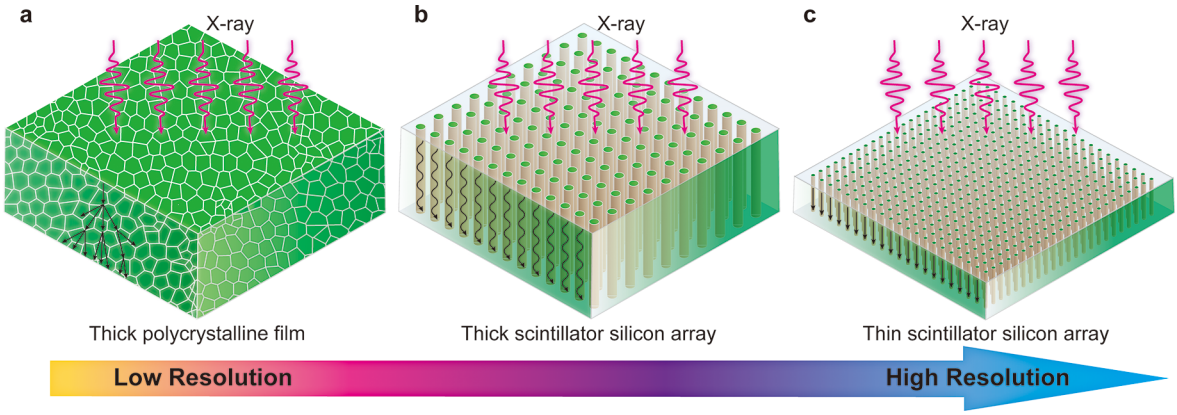

[a](a) Low X-ray imaging resolution due to the light scattering of particles in the thick polycrystalline scintillator screen, (b) the optical waveguide effect of the thick silicon array scintillator screen, which reduces light scattering and improves the spatial resolution, and (c) a thin silicon array scintillator screen with lower light scattering that enables a higher spatial resolution.

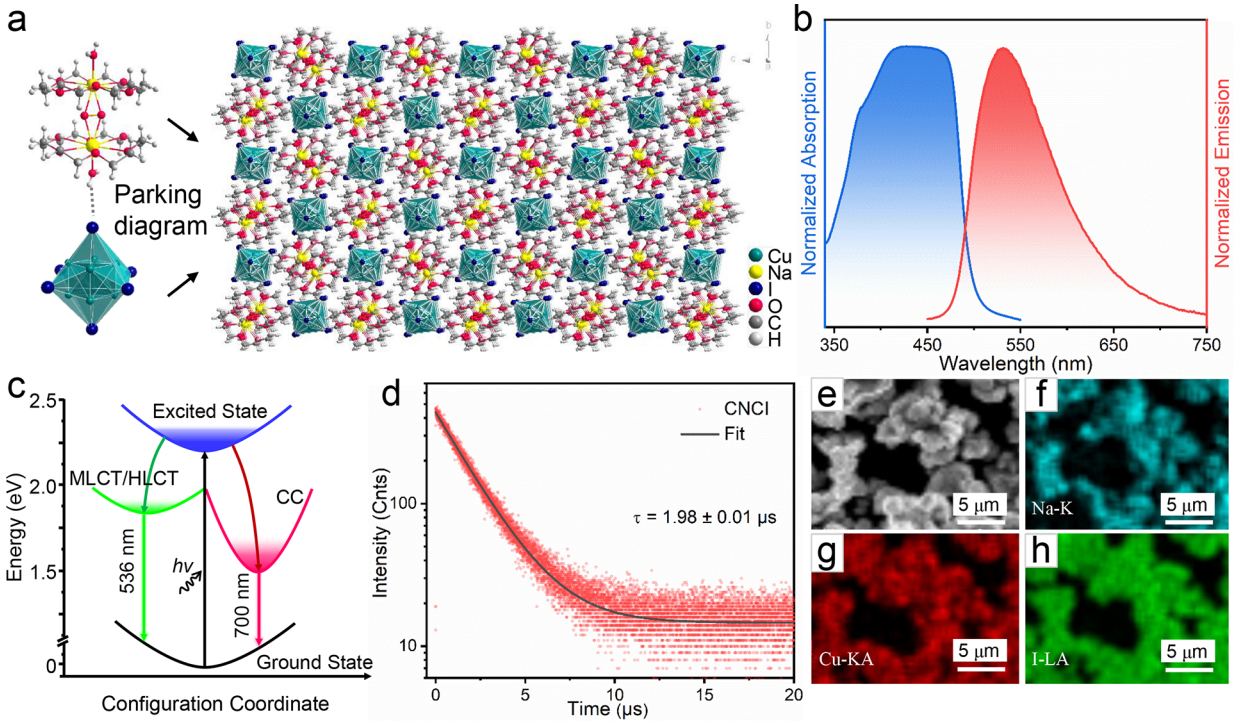

Figure 1. (a) Structure of 0D (18-crown-6)$_2$Na$_2$(H$_2$O)$_3$Cu$_4$I$_6$ (blue octahedrons: $[Cu_4I_6]^{2-}$ octahedrons). (b) Absorption and photoluminescence (λ_{ex} = 420 nm) spectra of CNCI powder. (c) Schematic diagram of photophysical processes. (d) PL decay curve of CNCI under 450 nm excitation and monitoring wavelength of 535 nm. (e–h) Energy dispersive X-ray spectroscopy (EDS) elemental mapping of CNCI powders with the scale bar of 5 μm.

screens, they consistently exhibit a lower spatial imaging resolution compared with other materials at the same light yield (Scheme 1a). Therefore, strategies that can improve the spatial resolution of X-ray scintillation screens to suppress light scattering are highly desirable. Recently, it has been reported that scintillator arrays embedded in anodized aluminum oxide (AAO) templates possess optical waveguide structures that confine light in high refractive index pores and reduce optical cross-talk, thus enabling excellent scintillation and X-ray imaging performance.[27,28] Compared with AAO templates, silicon templates with a larger area and tunable micropores can effectively obviate solution-processed pixelated scintillator fabrication methods. Furthermore, although light management engineering has proven to be effective in improving imaging resolution, little attention has been paid to the effect of template structure on imaging resolution. We conclude that thinner silicon templates with smaller pore diameters can significantly reduce light scattering and spreading, improving the resolution of X-ray imaging screens (Scheme 1b,c).

Herein, we present a zero-dimensional organic copper iodide, CNCI, with a high X-ray absorption cross-section and near-unity PLQY as a new high-performance X-ray imaging scintillator. The CNCI scintillator shows high X-ray sensitivity, including a high light yield of 87,500 photons/MeV

https://doi.org/10.1021/acscentsci.2c01495
ACS Cent. Sci. 2023, 9, 668–674

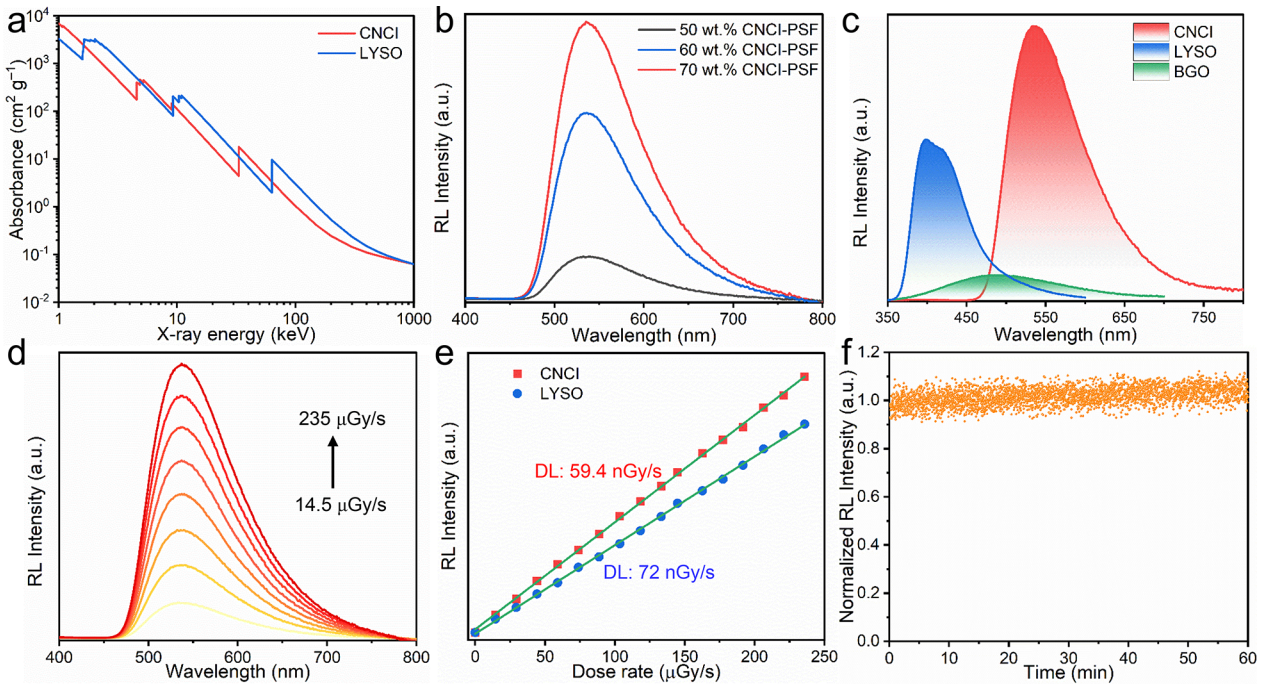

Figure 2. (a) Absorption coefficients of CNCI and LYSO under high-energy radiation. (b) Dependence of the radioluminescence intensity of CNCI-PSF films on the concentration of CNCI. (c) Radiation luminance spectra of CNCI films, LYSO:Ce, and BGO single crystals under the same X-ray illumination. (d) Radioluminescence spectra of 70 wt.% CNCI-PSF film under X-ray radiation at different dose rates. (e) Radioluminescence intensity of 70 wt.% CNCI-PSF film and LYSO:Ce as a linear function of dose rate. (f) Radioluminescence stability under continuous X-ray illumination at a dose of 2.4 mGy/s.

and an ultralow detection limit of 59.4 nGy/s. More importantly, a pixelated CNCI-silicon array scintillation screen was successfully prepared by a facile solution synthesis route using a silicon template. Benefiting from the highly reduced light scattering and light confinement of the arrayed scintillator, the pixelated scintillator array exhibits a remarkably high spatial resolution of 24.8 lp/mm, demonstrating the distinct advantages of organic copper iodide materials in high-performance X-ray imaging applications.

Crystals of $(18\text{-crown-}6)_2Na_2(H_2O)_3Cu_4I_6$ (CNCI) were synthesized according to the ball milling method.[25] CNCI crystallizes in a monoclinic space group (Figure 1a), with isolated $[Cu_4I_6]^{2-}$ tetrahedrons surrounded by $(18\text{-crown-}6)_2Na_2(H_2O)_3^{2+}$ cations. The structure of CNCI crystals and powder samples was well confirmed. The powder X-ray diffraction (XRD) pattern matches well with the standard reference (Figure S1), and EDS elemental mapping shows that Na, Cu, and I were homogeneously distributed in a crystal sample (Figures 1e–h and S2–S3). As shown in Figures 1b and S4, CNCI powder exhibited an absorption spectrum from 375 to 500 nm and a broad emission band from 450 to 750 nm centered at 536 nm, with a full width at half-maximum (FWHM) of 110 nm. It is worth noting that CNCI exhibits asymmetric emission spectra that correspond to the double emission of two different energy states: emission induced by metal–ligand charge transfer or halide-ligand charge transfer (MLCT/HLCT) at 536 nm and emission induced by a cluster center (CC) at 700 nm (Figure 1c). In addition, the PLQY (Figure S5) of the greenish-yellow emission was measured to be about 94%, which might originate from individual $[Cu_4I_6]^{-2}$ quantum dots exhibiting a strong quantum confinement effect due to the 0D electronic nature of CNCI.[25,29,30] The PL lifetime of the as-prepared CNCI crystals at 535 nm was then recorded by the time-correlated single-photon counting (TCSPC) method; the brief lifetime of 1.98 μs is shorter than that of most reported low-dimensional organic metal halides (Figure 1d).[31−33] Due to their negligible self-absorption, ultrabroad emission spectrum, nearly 100% PLQY, and short luminescence lifetime, the CNCI crystals position them as a promising scintillator material.

With respect to scintillation performance, the absorption spectrum of CNCI was calculated and found to be comparable to that of commercial scintillators (LYSO) over a broad range of X-ray detection regions (4–60 keV) (Figure 2a).[34] CNCI-polysulfone (CNCI-PSF) composite films were first engineered by encapsulating different weight percentages of CNCI particles into a polysulfone matrix. As shown in Figure 2b, the radioluminescence (RL) spectra of the CNCI-PSF composite films showed peaks similar to those observed in the corresponding PL spectra, indicating the same luminescence mechanism under UV and X-ray irradiation. Moreover, the RL intensity gradually increased as the doping ratio of CNCI in PSF increased from 50 to 70 wt.% due to more efficient X-ray absorption at higher concentrations. According to Figure S6, the attenuation efficiencies of 500 μm LYSO crystal and CNCI-PSF film are 90% and 72%, respectively. By normalizing the absorption of X-rays by the two scintillators, it can be ensured that the CNCI absorbs the same X-rays photons as the commercial LYSO film. The light yield (~109,000 photons/MeV) of the 70 wt.% CNCI-PSF film was calculated by integrating the X-ray-induced RL spectra and comparing the results with those obtained for the references LYSO:Ce (33,000 photons per MeV) and $Bi_4Ge_3O_{12}$ (BGO) (10,000 photons per MeV) (Figure 2c). The light yield of CNCI significantly outperforms that of previously reported $CsPbBr_3$ nanocrystals (~21,000 photons/MeV),[9] Rb_2CuBr_3 (~91,000

https://doi.org/10.1021/acscentsci.2c01495
ACS Cent. Sci. 2023, 9, 668−674

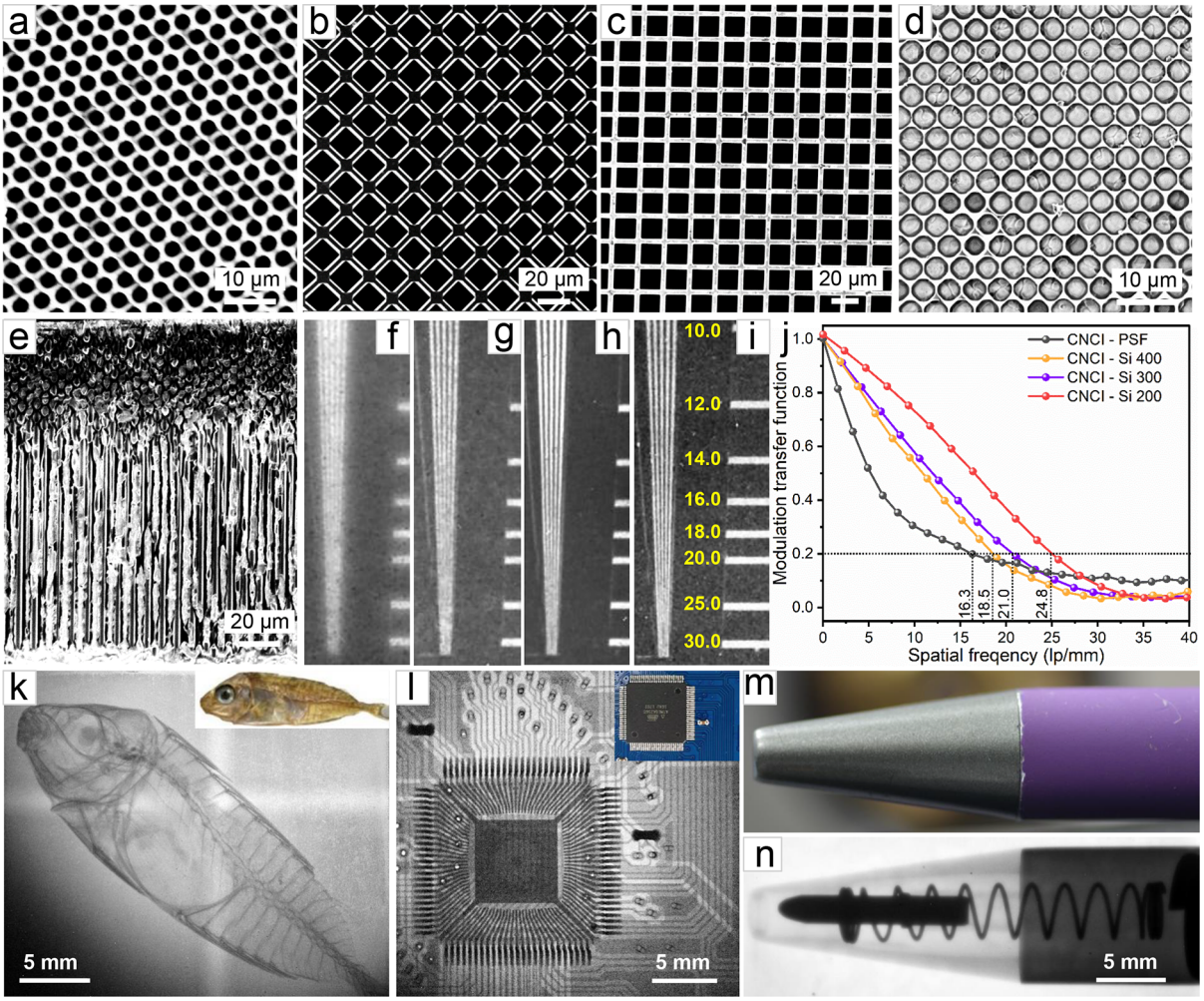

Figure 3. (a–c) Top-view SEM images of silicon 200, 300, and 400 templates, respectively. (d) Top-view and (e) cross-sectional SEM image of as-prepared CNCI-silicon 200 array scintillator. Two-dimensional X-ray images of a test-pattern plate based on (f) CNCI-PSF film, (g) CNCI-Si 400, (h) CNCI-Si 300, and (i) CNCI-Si 200 films. (j) MTF of CNCI-PSF and CNCI-Si array films measured by the slanted-edge method. Photographs (insets) and X-ray images of (k) fish, (l) circuit board, and (m, n) pen.

photons/MeV),[14] and $(C_{38}H_{34}P_2)MnBr_4$ (~80,000 photons/MeV)[16] and is even higher than that of some commercial scintillators (~CsI:Tl: 66,000 photons/MeV; GOS: ~60,000 photons/MeV),[35,36] demonstrating the material's high potential in medical radiography and security screening.

The RL intensity of the 70 wt.% CNCI-PSF film scaled linearly with the X-ray dose rate from 14.5 μGy/s to 235 μGy/s (Figure 2d). A low detection limit of 59.4 nGy/s was calculated from the slope of the fitting line in Figure 2e and Figure S7 at a signal-to-noise ratio of 3, which is lower than that obtained for the LYSO scintillator (72 nGy/s) and nearly 92 times lower than the dose rate required for a standard medical X-ray diagnosis (5.5 μGy/s). Moreover, the RL intensity of the 70 wt.% CNCI-PSF film remained at ~100% of the initial value over 1 h of continuous X-ray irradiation at a dose rate of 2.4 mGy/s (total dose, 8.6 Gy) (Figure 2f), demonstrating the high structural and radiation stability of the CNCI scintillator during extended radiation exposure.

To further validate the potential of CNCI as a scintillation material for practical X-ray imaging, we encapsulated CNCI in polysulfone polymer film and silicon membranes. X-ray imaging tests were then performed on a home-built imaging system consisting of an X-ray source, an imaging object, a reflector, and a camera. As shown in Figures 3f and S8, a distinguishable line spacing between 14.3 and 16.6 lp/mm was obtained using 70 wt.% CNCI-PSF scintillation films measuring 100 μm in thickness. A spatial resolution of 16.3 lp/mm was calculated at a modulation transfer function (MTF) value of 20%, consistent with the resolution limit observed from the standard line-pair card (Figure 3j).

More importantly, the X-ray imaging resolution of CNCI was further improved by confining the material in silicon membranes with controllable pore size and structure due to guiding the scintillating lights in high refractive index pores. The CNCI scintillator crystals were well encapsulated in the pores of silicon membranes of different thicknesses by using the impregnation method (Figures 3a–c and S9). Top and cross-sectional SEM images (Figures 3d,e, and S10–S12) show that the pores of the silicon membranes were completely filled with CNCI crystals, and one-dimensional scintillator rod arrays with different diameters (17 μm, 17 μm, and 2.8 μm for CNCI-Si 400, CNCI-Si 300, and CNCI-Si 200) were well formed. Interestingly, the X-ray imaging resolution was highly increased from 16.3 lp/mm for the CNCI-PSF films to 18.5 lp/mm for the CNCI-Si 400 screen (Figures 3g,j, and S13). Moreover, the imaging resolution of the pixelated CNCI-

https://doi.org/10.1021/acscentsci.2c01495
ACS Cent. Sci. 2023, 9, 668–674

silicon array scintillation screen could be further improved by adjusting the thickness and pore size of the Si template. As shown in Figures 3h and S14, the spatial imaging resolution of CNCI-Si 300 films was improved to 20.3 lp/mm when the thickness of the silicon template was reduced to 300 μm. Further decreasing the thickness and hole diameter of the silicon templates led to a remarkably increased spatial resolution of 24.8 lp/mm for CNCI-Si 200 films with a thickness of 200 μm and a hole diameter of 2.8 μm (Figures 3i and S15). We found that the light output of the CNCI-Si scintillator screens decreases as the silicon template becomes thinner due to the reduced X-ray absorption by the CNCI-Si screens (Table S1). In addition, the light output of CNCI-Si scintillator screens is lower than that of pure CNCI films. This is because the silicon template will also absorb the light emitted by the CNCI scintillator under X-ray radiation. Therefore, we conclude that the thickness and hole diameter of the silicon template can significantly affect the light propagation process of the scintillators at the microscale domain. By decreasing the thickness and pore diameter of the silicon template, more efficient light propagation will occur. This is the main reason for the increased spatial resolution observed on CNCI-Si 200 scintillators screens. Based on the ultrahigh resolution of the pixelated CNCI-silicon array scintillation screen, we performed a series of imaging experiments to demonstrate their high practical application value in radiography. The skeleton of a small fish, the internal circuitry of a microchip, and the spring inside a ballpoint pen were clearly distinguished by a well-defined boundary under X-ray irradiation by using the CNCI-Si 200 scintillation screen (Figure 3k). These results demonstrate the great potential of the CNCI-Si array scintillation films in biological imaging and nondestructive detection (Figure 3l–n).

In summary, we successfully developed novel organometallic halide X-ray scintillators based on $(18\text{-crown-}6)_2Na_2(H_2O)_3Cu_4I_6$ with negligible self-absorption and near-unity green-light emission. The CNCI scintillators exhibited desirable X-ray sensitivity, including an ultrahigh light yield of ~109,000 photons/MeV and an ultralow detection limit of 59.4 nGy/s, which is approximately 92 times lower than the dosage for a standard medical diagnosis. In addition, a facile solution-embedding strategy was proposed to fabricate an array scintillation screen based on silicon membranes. We found that the thickness and pore diameter of the silicon template can significantly influence the spatial resolution of the CNCI-Si scintillator array screen. As a consequence, a CNCI-Si 200 scintillator array demonstrated excellent light propagation efficiency in micron-size pores and achieved the highest spatial imaging resolution of up to 24.8 lp/mm. Our study is a pioneering effort in the structure-to-performance correlation of scintillator arrays designed for use in X-ray imaging and may stimulate the exploration of low-cost, high-performance, eco-friendly metal halide materials as radiation scintillators.

■ ASSOCIATED CONTENT

Supporting Information

The Supporting Information is available free of charge at https://pubs.acs.org/doi/10.1021/acscentsci.2c01495.

Experimental methods; additional X-ray imaging data; composition and structural characterization by XRD, UV–vis, and SEM (PDF)

■ AUTHOR INFORMATION

Corresponding Author

Omar F. Mohammed − *Advanced Membranes and Porous Materials Center, Division of Physical Science and Engineering, King Abdullah University of Science and Technology, Thuwal 23955-6900, Kingdom of Saudi Arabia; KAUST Catalysis Center, Division of Physical Sciences and Engineering, King Abdullah University of Science and Technology, Thuwal 23955-6900, Kingdom of Saudi Arabia;* orcid.org/0000-0001-8500-1130; Email: omar.abdelsaboor@kaust.edu.sa

Authors

Hong Wang − *Advanced Membranes and Porous Materials Center, Division of Physical Science and Engineering, King Abdullah University of Science and Technology, Thuwal 23955-6900, Kingdom of Saudi Arabia; KAUST Catalysis Center, Division of Physical Sciences and Engineering, King Abdullah University of Science and Technology, Thuwal 23955-6900, Kingdom of Saudi Arabia*

Jian-Xin Wang − *Advanced Membranes and Porous Materials Center, Division of Physical Science and Engineering, King Abdullah University of Science and Technology, Thuwal 23955-6900, Kingdom of Saudi Arabia;* orcid.org/0000-0002-7838-5575

Xin Song − *KAUST Catalysis Center, Division of Physical Sciences and Engineering, King Abdullah University of Science and Technology, Thuwal 23955-6900, Kingdom of Saudi Arabia*

Tengyue He − *Advanced Membranes and Porous Materials Center, Division of Physical Science and Engineering, King Abdullah University of Science and Technology, Thuwal 23955-6900, Kingdom of Saudi Arabia; KAUST Catalysis Center, Division of Physical Sciences and Engineering, King Abdullah University of Science and Technology, Thuwal 23955-6900, Kingdom of Saudi Arabia*

Yang Zhou − *Advanced Membranes and Porous Materials Center, Division of Physical Science and Engineering, King Abdullah University of Science and Technology, Thuwal 23955-6900, Kingdom of Saudi Arabia; KAUST Catalysis Center, Division of Physical Sciences and Engineering, King Abdullah University of Science and Technology, Thuwal 23955-6900, Kingdom of Saudi Arabia*

Osama Shekhah − *Advanced Membranes and Porous Materials Center, Division of Physical Science and Engineering, King Abdullah University of Science and Technology, Thuwal 23955-6900, Kingdom of Saudi Arabia;* orcid.org/0000-0003-1861-9226

Luis Gutiérrez-Arzaluz − *Advanced Membranes and Porous Materials Center, Division of Physical Science and Engineering, King Abdullah University of Science and Technology, Thuwal 23955-6900, Kingdom of Saudi Arabia; KAUST Catalysis Center, Division of Physical Sciences and Engineering, King Abdullah University of Science and Technology, Thuwal 23955-6900, Kingdom of Saudi Arabia;* orcid.org/0000-0001-8971-9377

Mehmet Bayindir − *Center for Hybrid Nanostructures, University of Hamburg, 22761 Hamburg, Germany;* orcid.org/0000-0003-0233-6870

Mohamed Eddaoudi − *Advanced Membranes and Porous Materials Center, Division of Physical Science and Engineering, King Abdullah University of Science and*

https://doi.org/10.1021/acscentsci.2c01495
ACS Cent. Sci. 2023, 9, 668−674

Technology, Thuwal 23955-6900, Kingdom of Saudi Arabia; orcid.org/0000-0003-1916-9837

Osman M. Bakr − *KAUST Catalysis Center, Division of Physical Sciences and Engineering, King Abdullah University of Science and Technology, Thuwal 23955-6900, Kingdom of Saudi Arabia;* orcid.org/0000-0002-3428-1002

Complete contact information is available at: https://pubs.acs.org/10.1021/acscentsci.2c01495

Notes

The authors declare no competing financial interest.

■ ACKNOWLEDGMENTS

This work was supported by the King Abdullah University of Science and Technology (KAUST).

■ REFERENCES

(1) Zhou, Y.; Chen, J.; Bakr, O. M.; Mohammed, O. F. Metal Halide Perovskites for X-ray Imaging Scintillators and Detectors. *ACS Energy Lett.* **2021**, *6* (2), 739−768.

(2) Wu, H. D.; Ge, Y. S.; Niu, G. D.; Tang, J. Metal Halide Perovskites for X-Ray Detection and Imaging. *Matter* **2021**, *4* (1), 144−163.

(3) Heo, J. H.; Shin, D. H.; Park, J. K.; Kim, D. H.; Lee, S. J.; Im, S. H. High-Performance Next-Generation Perovskite Nanocrystal Scintillator for Nondestructive X-Ray Imaging. *Adv. Mater.* **2018**, *30* (40), 1801743.

(4) Roques-Carmes, C.; Rivera, N.; Ghorashi, A.; Kooi, S. E.; Yang, Y.; Lin, Z.; Beroz, J.; Massuda, A.; Sloan, J.; Romeo, N.; Yu, Y.; Joannopoulos, J. D.; Kaminer, I.; Johnson, S. G.; Soljacic, M. A Framework for Scintillation in Nanophotonics. *Science* **2022**, *375* (6583), No. eabm9293.

(5) Ma, W. B.; Su, Y. R.; Zhang, Q. S.; Deng, C.; Pasquali, L.; Zhu, W. J.; Tian, Y.; Ran, P.; Chen, Z.; Yang, G. Y.; Liang, G. J.; Liu, T. Y.; Zhu, H. M.; Huang, P.; Zhong, H. Z.; Wang, K. W.; Peng, S. Q.; Xia, J. L.; Liu, H. F.; Liu, X.; Yang, Y. M. Thermally Activated Delayed Fluorescence (TADF) Organic Molecules for Efficient X-ray Scintillation and Imaging. *Nat. Mater.* **2022**, *21* (7), 836−836.

(6) Wang, J. X.; Gutierrez-Arzaluz, L.; Wang, X. J.; He, T. Y.; Zhang, Y. H.; Eddaoudi, M.; Bakr, O. M.; Mohammed, O. F. Heavy-atom Engineering of Thermally Activated Delayed Fluorophores for High-performance X-ray Imaging Scintillators. *Nat. Photonics* **2022**, *16*, 869−875.

(7) Chen, Q. S.; Wu, J.; Ou, X. Y.; Huang, B. L.; Almutlaq, J.; Zhumekenov, A. A.; Guan, X. W.; Han, S. Y.; Liang, L. L.; Yi, Z. G.; Li, J.; Xie, X. J.; Wang, Y.; Li, Y.; Fan, D. Y.; Teh, D. B. L.; All, A. H.; Mohammed, O. F.; Bakr, O. M.; Wu, T.; Bettinelli, M.; Yang, H. H.; Huang, W.; Liu, X. G. All-inorganic Perovskite Nanocrystal Scintillators. *Nature* **2018**, *561* (7721), 88−93.

(8) Clinckemalie, L.; Valli, D.; Roeffaers, M. B. J.; Hofkens, J.; Pradhan, B.; Debroye, E. Challenges and Opportunities for $CsPbBr_3$ Perovskites in Low- and High-Energy Radiation Detection. *ACS Energy Lett.* **2021**, *6* (4), 1290−1314.

(9) Zhang, Y. H.; Sun, R. J.; Qi, X. Y.; Fu, K. F.; Chen, Q. S.; Ding, Y. C.; Xu, L. J.; Liu, L. M.; Han, Y.; Malko, A. V.; Liu, X. G.; Yang, H. H.; Bakr, O. M.; Liu, H.; Mohammed, O. F. Metal Halide Perovskite Nanosheet for X-ray High-Resolution Scintillation Imaging Screens. *ACS Nano* **2019**, *13* (2), 2520−2525.

(10) Ma, W.; Jiang, T.; Yang, Z.; Zhang, H.; Su, Y.; Chen, Z.; Chen, X.; Ma, Y.; Zhu, W.; Yu, X.; Zhu, H.; Qiu, J.; Liu, X.; Xu, X.; Yang, Y. Highly Resolved and Robust Dynamic X-Ray Imaging Using Perovskite Glass-Ceramic Scintillator with Reduced Light Scattering. *Adv. Sci.* **2021**, *8* (15), 2003728.

(11) Zheng, J. X.; Zeng, Y.; Wang, J. J.; Sun, C. H.; Tang, B.; Wu, Y.; Zhang, Y.; Yi, Y. P.; Wang, N.; Zhao, Y.; Zhou, S. Y. Hydrogen-Rich 2D Halide Perovskite Scintillators for Fast Neutron Radiography. *J. Am. Chem. Soc.* **2021**, *143* (50), 21302−21311.

(12) Boyd, C. C.; Cheacharoen, R.; Leijtens, T.; McGehee, M. D. Understanding Degradation Mechanisms and Improving Stability of Perovskite Photovoltaics. *Chem. Rev.* **2019**, *119* (5), 3418−3451.

(13) Huang, H.; Bodnarchuk, M. I.; Kershaw, S. V.; Kovalenko, M. V.; Rogach, A. L. Lead Halide Perovskite Nanocrystals in the Research Spotlight: Stability and Defect Tolerance. *ACS Energy Lett.* **2017**, *2* (9), 2071−2083.

(14) Yang, B.; Yin, L. X.; Niu, G. D.; Yuan, J. H.; Xue, K. H.; Tan, Z. F.; Miao, X. S.; Niu, M.; Du, X. Y.; Song, H. S.; Lifshitz, E.; Tang, J. Lead-Free Halide Rb_2CuBr_3 as Sensitive X-Ray Scintillator. *Adv. Mater.* **2019**, *31* (44), 1904711.

(15) He, T. Y.; Zhou, Y.; Wang, X. J.; Yin, J.; Gutierrez-Arzaluz, L.; Wang, J. X.; Zhang, Y. H.; Bakr, O. M.; Mohammed, O. F. High-Performance Copper-Doped Perovskite-Related Silver Halide X-ray Imaging Scintillator. *ACS Energy Lett.* **2022**, *7* (8), 2753−2760.

(16) Xu, L. J.; Lin, X. S.; He, Q. Q.; Worku, M.; Ma, B. W. Highly Efficient Eco-friendly X-ray Scintillators Based on an Organic Manganese Halide. *Nat. Commun.* **2020**, *11* (1), 4329.

(17) He, Q. Q.; Zhou, C. K.; Xu, L. J.; Lee, S. J.; Lin, X. S.; Neu, J.; Worku, M.; Chaaban, M.; Ma, B. W. Highly Stable Organic Antimony Halide Crystals for X-ray Scintillation. *ACS Mater. Lett.* **2020**, *2* (6), 633−638.

(18) Cao, J. T.; Guo, Z.; Zhu, S.; Fu, Y. Y.; Zhang, H.; Wang, Q.; Gu, Z. J. Preparation of Lead-free Two-Dimensional-Layered $(C_8H_{17}NH_3)_2SnBr_4$ Perovskite Scintillators and Their Application in X-ray Imaging. *ACS Appl. Mater. Interfaces* **2020**, *12* (17), 19797−19804.

(19) Zhang, Z. Z.; Wei, J. H.; Luo, J. B.; Wang, X. D.; He, Z. L.; Kuang, D. B. Large-Area Laminar TEA_2MnI_4 Single-Crystal Scintillator for X-ray Imaging with Impressive High Resolution. *ACS Appl. Mater. Interfaces* **2022**, *14*, 47913−47921.

(20) Lian, L. Y.; Zheng, M. Y.; Zhang, W. Z.; Yin, L. X.; Du, X. Y.; Zhang, P.; Zhang, X. W.; Gao, J. B.; Zhang, D. L.; Gao, L.; Niu, G. D.; Song, H. S.; Chen, R.; Lan, X. Z.; Tang, J.; Zhang, J. B. Efficient and Reabsorption-Free Radioluminescence in $Cs_3Cu_2I_5$ Nanocrystals with Self-Trapped Excitons. *Adv. Sci.* **2020**, *7* (11), 2000195.

(21) Zhao, X.; Niu, G. D.; Zhu, J. S.; Yang, B.; Yuan, J. H.; Li, S. R.; Gao, W. R.; Hu, Q. S.; Yin, L. X.; Xue, K. H.; Lifshitz, E.; Miao, X. S.; Tang, J. All-Inorganic Copper Halide as a Stable and Self-Absorption-Free X-ray Scintillator. *J. Phys. Chem. Lett.* **2020**, *11* (5), 1873−1880.

(22) Li, N.; Xu, Z. W.; Xiao, Y. R.; Liu, Y. C.; Yang, Z.; Liu, S. Z. Flexible, High Scintillation Yield $Cu_3Cu_2I_5$ Film Made of Ball-Milled Powder for High Spatial Resolution X-Ray Imaging. *Adv. Opt. Mater.* **2022**, *10* (5), 2102232.

(23) Lian, L. Y.; Wang, X.; Zhang, P.; Zhu, J. S.; Zhang, X. W.; Gao, J. B.; Wang, S.; Liang, G. J.; Zhang, D. L.; Gao, L.; Song, H. S.; Chen, R.; Lan, X. Z.; Liang, W. X.; Niu, G. D.; Tang, J.; Zhang, J. B. Highly Luminescent Zero-Dimensional Organic Copper Halides for X-ray Scintillation. *J. Phys. Chem. Lett.* **2021**, *12* (29), 6919−6926.

(24) Xu, T. T.; Li, Y. Y.; Nikl, M.; Kucerkova, R.; Zhou, Z. Y.; Chen, J.; Sun, Y. Y.; Niu, G. D.; Tang, J.; Wang, Q.; Ren, G. H.; Wu, Y. T. Lead-Free Zero-Dimensional Organic-Copper(I) Halides as Stable and Sensitive X-ray Scintillators. *ACS Appl. Mater. Interfaces* **2022**, *14* (12), 14157−14164.

(25) Huang, J. L.; Su, B. B.; Song, E. H.; Molokeev, M. S.; Xia, Z. G. Ultra-Broad-Band-Excitable Cu(I)-Based Organometallic Halide with Near-Unity Emission for Light-Emitting Diode Applications. *Chem. Mater.* **2021**, *33* (12), 4382−4389.

(26) Zhao, W.; Wang, Y.; Guo, Y.; Suh, Y. D.; Liu, X. Color-Tunable and Stable Copper Iodide Cluster Scintillators for Efficient X-Ray Imaging. *Adv. Sci.* **2023**, *10*, 2205526.

(27) Zhao, X.; Jin, T.; Gao, W.; Niu, G.; Zhu, J.; Song, B.; Luo, J.; Pan, W.; Wu, H.; Zhang, M.; He, X.; Fu, L.; Li, Z.; Zhao, H.; Tang, J. Embedding $Cs_3Cu_2I_5$ Scintillators into Anodic Aluminum Oxide Matrix for High-Resolution X-Ray Imaging. *Adv. Opt. Mater.* **2021**, *9* (24), 2101194.

(28) Li, H.; Yang, H.; Yuan, R.; Sun, Z.; Yang, Y.; Zhao, J.; Li, Q.; Zhang, Z. Ultrahigh Spatial Resolution, Fast Decay, and Stable X-Ray Scintillation Screen through Assembling $CsPbBr_3$ Nanocrystals Arrays

in Anodized Aluminum Oxide. *Adv. Opt. Mater.* **2021**, *9* (24), 2101297.
(29) Yin, J.; Lei, Q.; Han, Y.; Bakr, O. M.; Mohammed, O. F. Luminescent Copper(I) Halides for Optoelectronic Applications. *Phys. Status Solidi-R* **2021**, *15* (12), 2100138.
(30) Jun, T.; Sim, K.; Iimura, S.; Sasase, M.; Kamioka, H.; Kim, J.; Hosono, H. Lead-Free Highly Efficient Blue-Emitting $Cs_3Cu_2I_5$ with 0D Electronic Structure. *Adv. Mater.* **2018**, *30* (43), 1804547.
(31) Li, S.; Xu, J.; Li, Z.; Zeng, Z.; Li, W.; Cui, M.; Qin, C.; Du, Y. One-Dimensional Lead-Free Halide with Near-Unity Greenish-Yellow Light Emission. *Chem. Mater.* **2020**, *32* (15), 6525−6531.
(32) Peng, H.; Wang, X.; Tian, Y.; Dong, T.; Xiao, Y.; Huang, T.; Guo, Y.; Wang, J.; Zou, B. Water-Stable Zero-Dimensional $(C_4H_9)_4NCuCl_2$ Single Crystal with Highly Efficient Broadband Green Emission. *J. Phys. Chem. Lett.* **2021**, *12* (28), 6639−6647.
(33) Jiang, T.; Ma, W.; Zhang, H.; Tian, Y.; Lin, G.; Xiao, W.; Yu, X.; Qiu, J.; Xu, X.; Yang, Y.; Ju, D. Highly Efficient and Tunable Emission of Lead-Free Manganese Halides toward White Light-Emitting Diode and X-Ray Scintillation Applications. *Adv. Funct. Mater.* **2021**, *31* (14), 2009973.
(34) Berger, M. J.; Hubbell, J. H.; Seltzer, S. M.; Chang, J.; Coursey, J. S.; Sukumar, R.; Zucker, D. S.; Olsen, K. XCOM: Photon Cross Sections Database: NIST Standard Reference Database 8 (NIST) 2013, https://www.nist.gov/pml/xcom-photon-cross-sectionsdatabase.
(35) Schotanus, P.; Kamermans, R.; Dorenbos, P. Scintillation Characteristics of Pure and Tl-Doped CsI Crystals. *IEEE Trans. Nucl. Sci.* **1990**, *37* (2), 177−182.
(36) van Eijk, C. W. E. Inorganic Scintillators in Medical Imaging. *Phys. Med. Biol.* **2002**, *47* (8), R85−R106.

https://doi.org/10.1021/acscentsci.2c01495
ACS Cent. Sci. 2023, 9, 668−674

Supporting Information

Copper Organometallic Iodide Arrays for Efficient X-ray Imaging Scintillators

Hong Wang, [†,‡] *Jian-Xin Wang,* [†] *Xin Song,* [‡] *Tengyue He,* [†,‡] *Yang Zhou,* [†,‡] *Osama Shekhah,* [†] *Luis Gutiérrez-Arzaluz,* [†,‡] *Mehmet Bayindir,* [§] *Mohamed Eddaoudi,* [†] *Osman M. Bakr,* [‡] *and Omar F. Mohammed*[*,†,‡]

[†] Advanced Membranes and Porous Materials Center, Division of Physical Science and Engineering, King Abdullah University of Science and Technology, Thuwal 23955-6900, Kingdom of Saudi Arabia

[‡] KAUST Catalysis Center, Division of Physical Sciences and Engineering, King Abdullah University of Science and Technology, Thuwal 23955-6900, Kingdom of Saudi Arabia

[§] Center for Hybrid Nanostructures, University of Hamburg, 22761 Hamburg, Germany

[*]Correspondence and requests for materials should be addressed to Omar F. Mohammed. (email: omar.abdelsaboor@kaust.edu.sa).

Chemicals and Materials. Copper (I) iodide (CuI, 99.999%), sodium iodide (NaI, 99%), 18-crown-6 ($C_{12}H_{24}O_6$, 99%), and Poly sulfone (average Mw ~350,000 by GPC) were purchased from Sigma Aldrich. H_3PO_2 (50 wt. %, in water) was received from Alfa Aesar. Chloroform (HPLC) was received from VWR Chemicals. Silicon templates were received from Smart MEMBRANES. These chemicals and reagents were used as received without further purification.

Synthesis of (18-crown-6)$_2$Na$_2$(H$_2$O)$_3$Cu$_4$I$_6$ (CNCI) Powder. CuI (2.5 mmol), NaI (2.5 mmol), H_3PO_2 (0.05 mL), and 18-crown-6 (5.0 mmol) were mixed in the mortar. The reaction mixture was ground for 10 min at room temperature to form the light green paste. The paste was dried naturally under the air.

Fabrication of CNCI-Polysulfone Composite Films. A calculated amount of CNCI powder was added in 2 mL of chloroform solvent and sonicated for ca. 2 min. Then, 200 mg Polysulfone (PSF) was added to the solution, followed by sonication for 2 min and shaking for 3 h to ensure that the powder and the polymer were well mixed. The viscous solution was carefully coated on the quartz plates (or in a 20 mL glass vial) and then covered with a beaker to allow the solvent to evaporate slowly in order to obtain the film with a uniform surface and good morphology.

Fabrication of CNCI-Si Pixelated Scintillating Screens. The CNCI powder was added to DMF solution and sonicated for about 5 min to dissolve completely. Then, a clean silicon template was added to the DMF solution and sonicated for 10 min to ensure that the solution was fully immersed in the silicon pores. The silicon template was removed from the solution and dried on a 100°C hot plate.

Characterizations of Samples. X-ray diffraction (XRD) patterns were recorded at room temperature using a Bruker D8 ADVANCE diffractometer with Cu Kα radiation (λ = 1.5406 Å). Scanning electron microscopy (SEM; Zeiss Auriga) with an energy-dispersive X-ray analyzer was used to analyze the morphologies and the chemical compositions of powder. Absorption spectra of the samples were measured using a UV-Vis spectrometer (PerkinElmer Lambda 950) equipped with an integrated sphere. The photoluminescence (PL) spectra were taken using a Horiba Fluoromax-4 spectrofluorometer with a photomultiplier (PMT-928). Photoluminescence quantum yield (PLQY) of the samples was measured using FS5 fluorescence spectrometer (Edinburgh Instruments). The excitation wavelength was set at 420 nm. Time-resolved photoluminescence was obtained through the TCSPC technique in a setup based on a modified microscope (Olympus IX71). The sample was excited at 450 nm with a pulsed diode laser (70 ps, HORIBA, Delta Diode) focused through a 10×, 0.4 NA microscope objective (Olympus); it was also used to collect the PL. Long-pass 493 nm and band-pass 535 nm filters (Newport) were used to reject scattered laser light and select the emission detection range. The filtered PL signal was focused on an avalanche photodiode (PDM series, MicroPhoton Devices). The histograms obtained were fitted with the SymphoTime64 software (PicoQuant) using the Levenberg–Marquardt iteration algorithm. The overall system's time resolution was better than 150 ps.

Radioluminescence (RL) Studies. The RL spectra were taken by a spectrometer (Horiba Fluoromax-4 spectrofluorometer) equipped with an X-ray tube (Tungsten target, Moxtek). The detection slit was set at 1 nm, and the X-ray outlet was set to 1 cm away from sample for all spectral measurements. The X-ray dose rate was controlled in a range from 3.43 μGy/s to 247

μGy/s by adjusting the input current and voltage values. All tests were carried out in a radiation-tight environment of lead-plate shielding.

Calculation of X-ray Detection Limit. The linear relationship between the RL intensity of the corresponding samples and the X-ray dose was obtained. The noise data was obtained in the absence of sample. The noise intensity value was statistically analyzed and fitted by the Gaussian function, whereby the FWHM was regarded as the average value of the noise. The detection limit in dose rate was derived from the slope of the fitting line, with a signal-to-noise ratio of 3.

Calculation of X-ray Light Yield. Commercial LYSO:Ce scintillator was used as a reference to estimate the light yield of the film samples. The films were fabricated to keep the same size (2×2 cm^2) and thickness (500 μm) as the LYSO:Ce reference sample, and RL curves were obtained using spectrometer under an identical configuration. Typically, the light yield of 70 wt. % CNCI-PSF film was estimated around 109,000 photons/MeV. BGO scintillator was used as another reference to cross-check the accuracy of this measurement method. The light yield is calculated by taking into the account the wavelength dependent detector efficiency (Hamamatsu, R928 PMT), X-ray absorption efficiencies of the LYSO:Ce and CNCI-PSF composite:

$$\mathrm{LY}_S = \mathrm{LY}_R \frac{\int \mathrm{I}_S(\lambda)\mathrm{d}\lambda}{\int \mathrm{I}_R(\lambda)\mathrm{d}\lambda} \frac{\int \mathrm{I}_R(\lambda)\mathrm{S}(\lambda)\mathrm{d}\lambda}{\int \mathrm{I}_S(\lambda)\mathrm{S}(\lambda)\mathrm{d}\lambda} \frac{\mathrm{XAE}_R}{\mathrm{XAE}_S}$$

Where LY_S and LY_R are sample and reference light yields, $\mathrm{I}_S(\lambda)$ and $\mathrm{I}_R(\lambda)$ are wavelength dependent radioluminescence intensities of sample and reference, $\mathrm{S}(\lambda)$ is wavelength dependent detector efficiency, XAE_S and XAE_R are X-ray attenuation efficiencies of sample and reference.

X-ray Image Collection and Process. A commercial camera (D7100, Nikon) was used to take images for X-ray imaging screen. The ISO, aperture, and shutter were set at 640, F3.5, and 10 for samples excited by X-ray. The voltage/current of the X-ray tube was set to 50 kV/200 μA (dose rate ≈ 5.2 mGy/s. The original X-ray images were further processed using the software Image J to remove the background of screen.

Calculation of X-ray Imaging Spatial Resolution. X-ray Imaging spatial resolution was calculated by Modulation transfer function (MTF) measurements. The MTF was calculated by the slanted edge method. Sharp edge X-ray imaging was carried out on the standard line-pair lead template with a thickness of ~ 0.5 mm. MTF operation on images through software ImageJ: Then the edge spread function (ESF) was derived from the edge image, and the line spread function (LSF) was derived from the derivation. Finally, the Fourier transform of LSF defined MTF. The summary was shown in the following formula:[1]

$$MTF(v) = F(LSF(x)) = F(\frac{dESF(x)}{dx})$$

Where ν was the spatial frequency. X is the position of pixels.

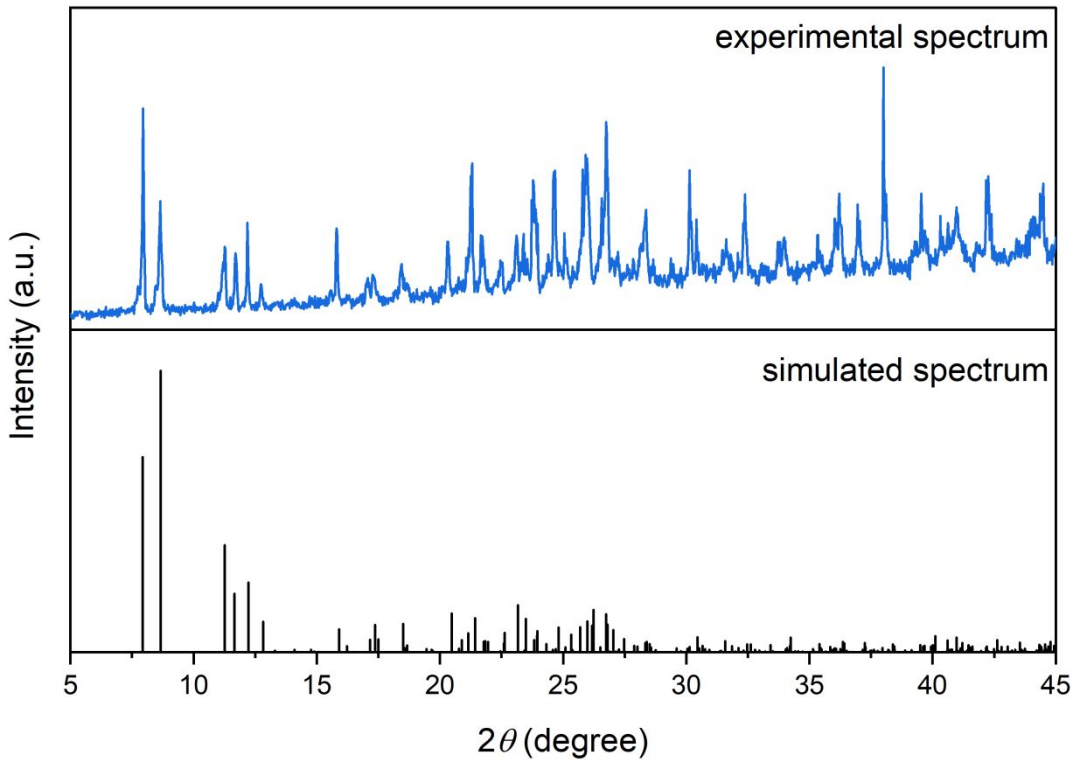

Figure S1. XRD patterns of the CNCI powders.

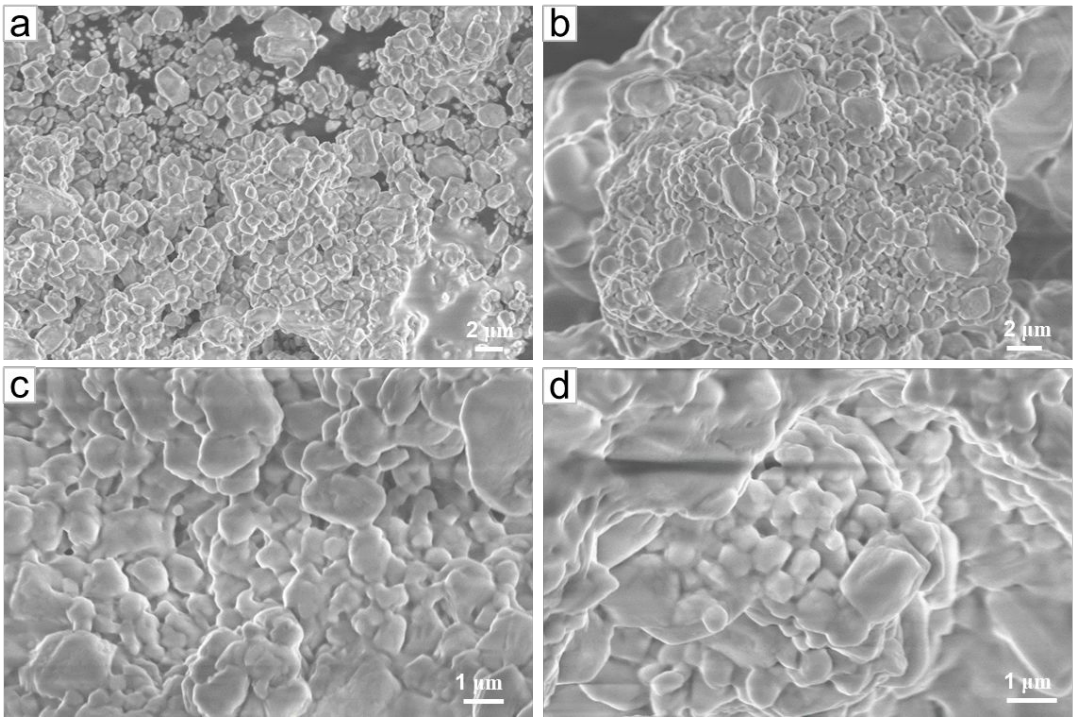

Figure S2. Scanning Electron Microscope (SEM) images of the as-synthesized CNCI powder with the scale bar of 2 µm (a-b) and 1 µm (c-d).

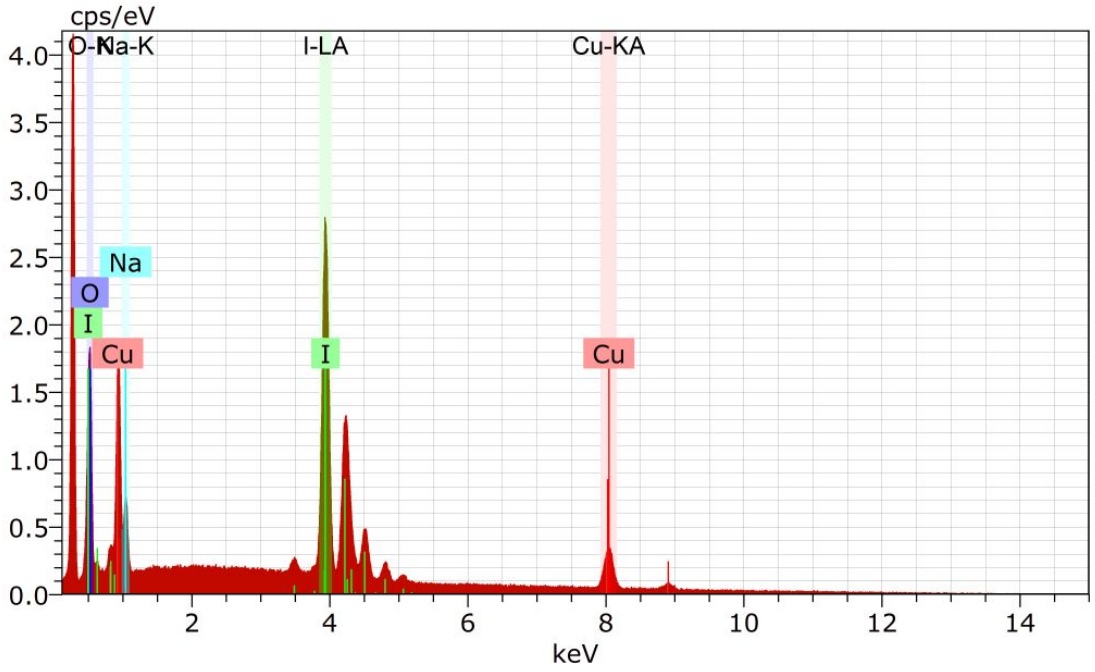

Figure S3. EDS spectra of the CNCI powders.

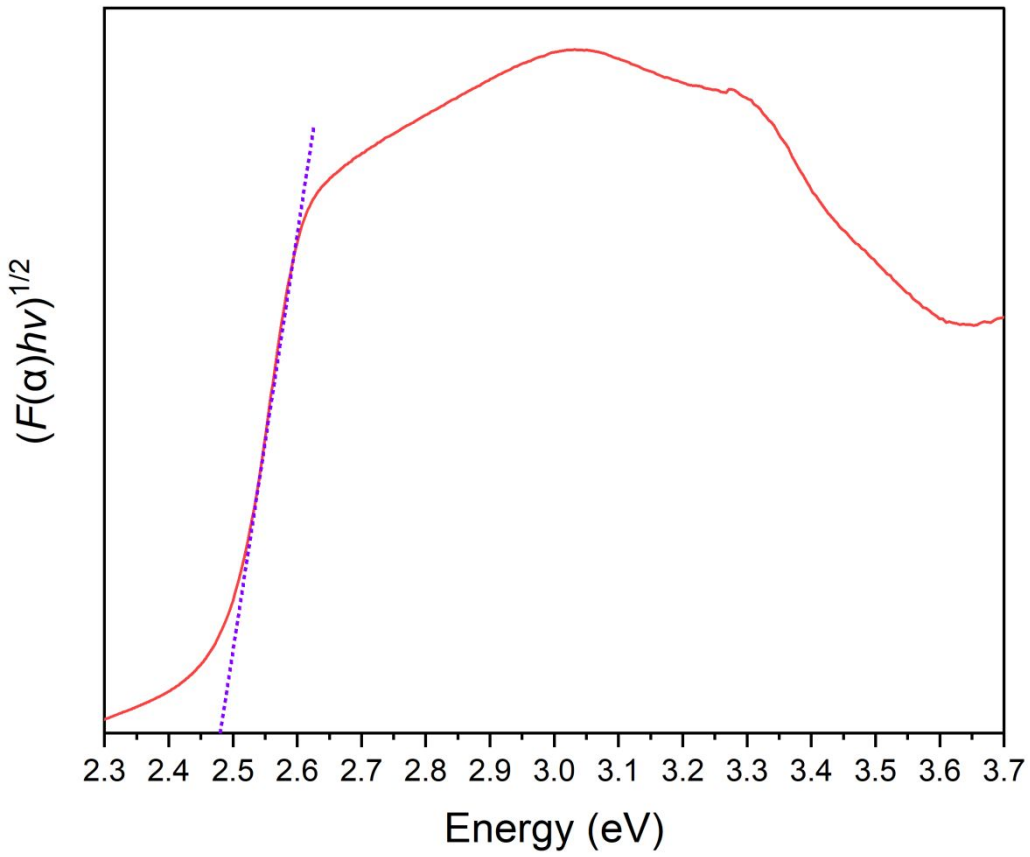

Figure S4. Kubelka-Munk equation applied to the absorbance spectrum of the CNCI powder.

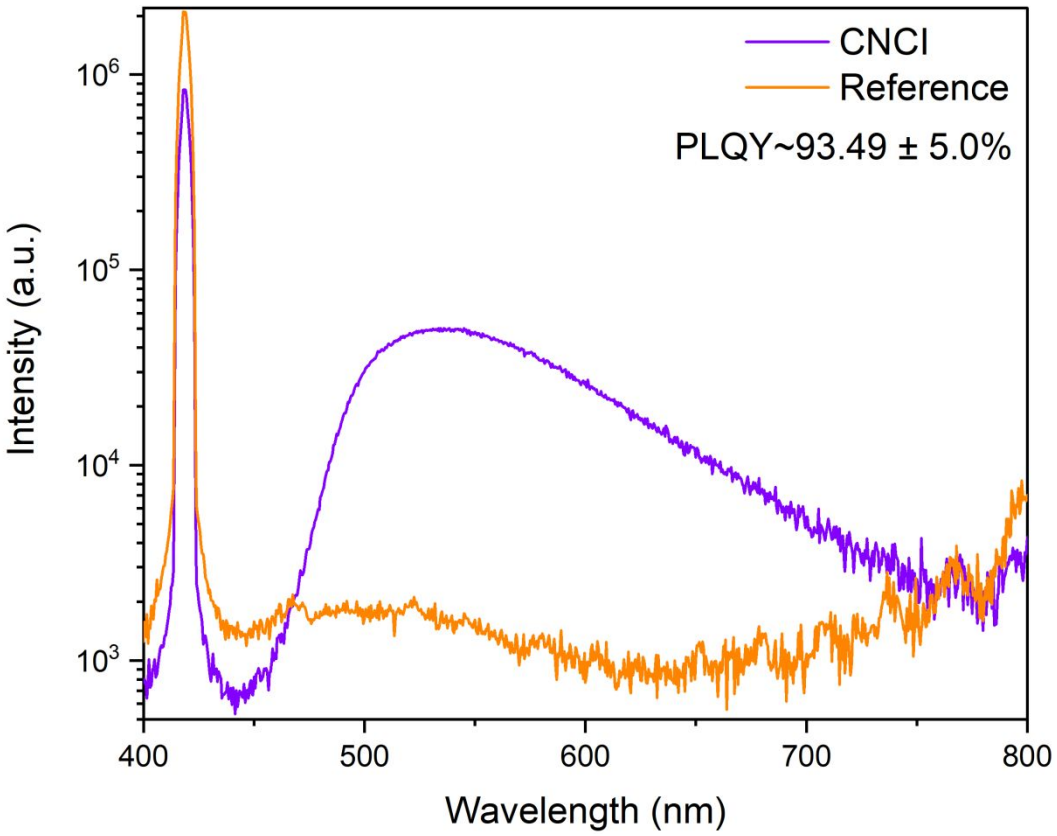

Figure S5. The PLQY spectra of CNCI powder. The reference curves were measured by placing a blank sample holder in the integrating sphere.

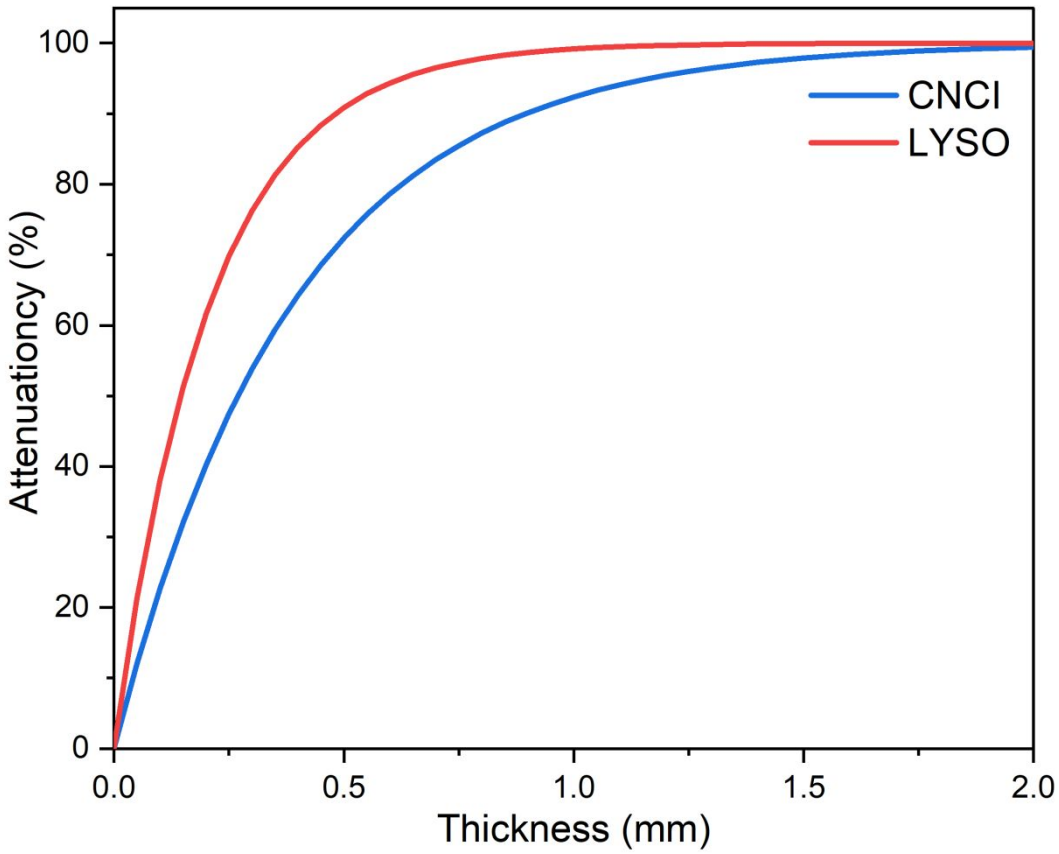

Figure S6. Attenuation efficiency of CNCI and LYSO for 40 keV X-ray photons versus thickness.

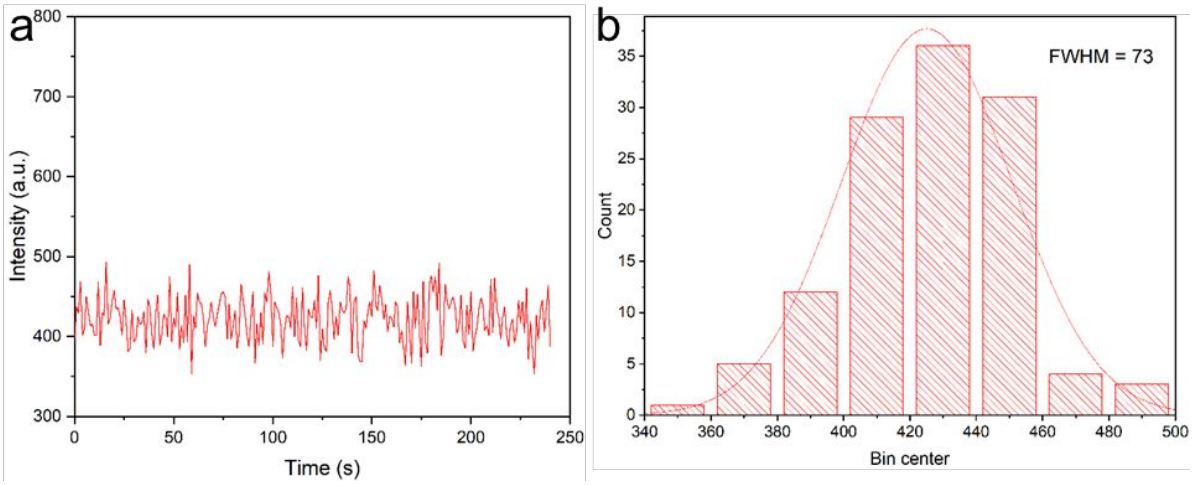

Figure S7. a) Background signal of the RL spectra. b) Background signal fitted with Gaussian function (Full width at half maximum: FWHM = 73).

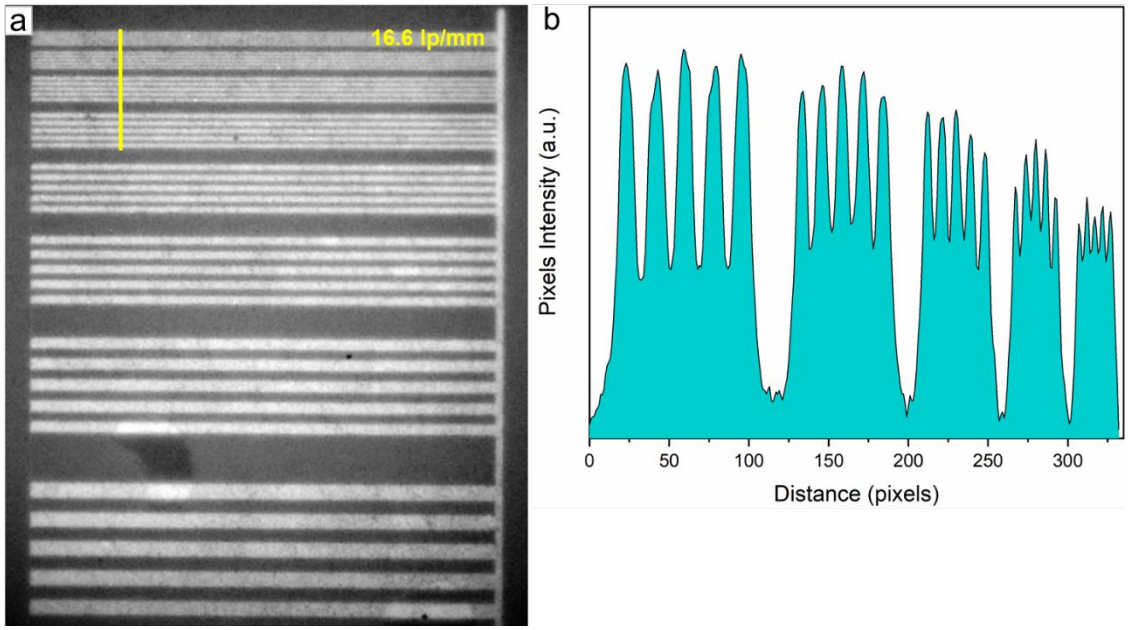

Figure S8. a) Spatial resolution of the 70 wt. % CNCI-PSF film was determined by a standard line-pair card (lp/mm). b) Spatial resolution measurement by the fitting of intensity spread profile.

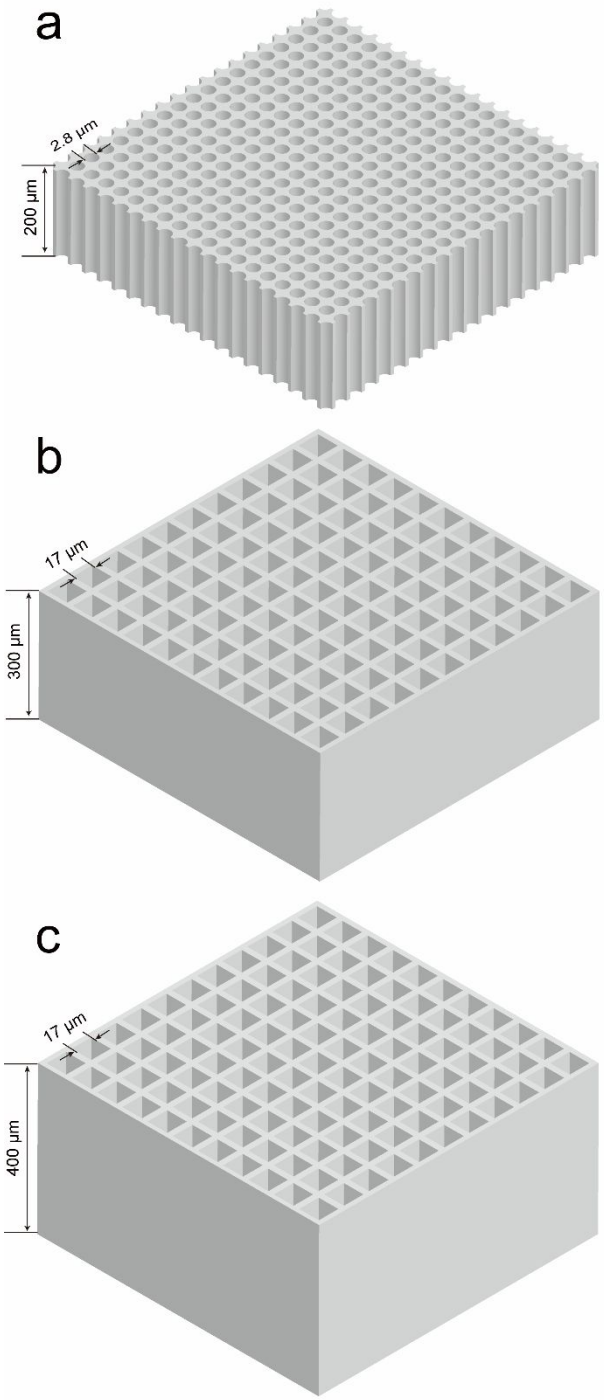

Figure S9. Schematic diagram of the structure and size of the (a) Si 200, (b) Si 300, and (c) Si 400 templates.

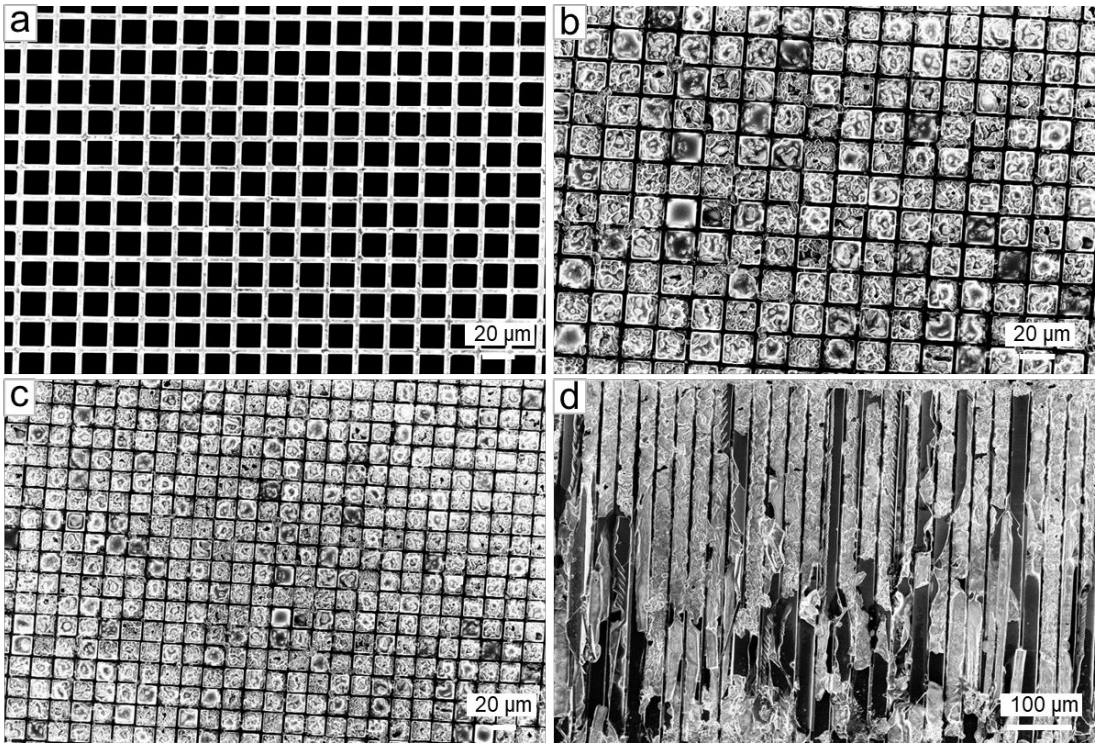

Figure S10. Surface SEM of Si 400 template, b) surface SEM of the CNCI-Si 400 arrays, c) surface SEM of the CNCI-Si 400 arrays, d) cross-sectional SEM image of CNCI-Si 400 arrays.

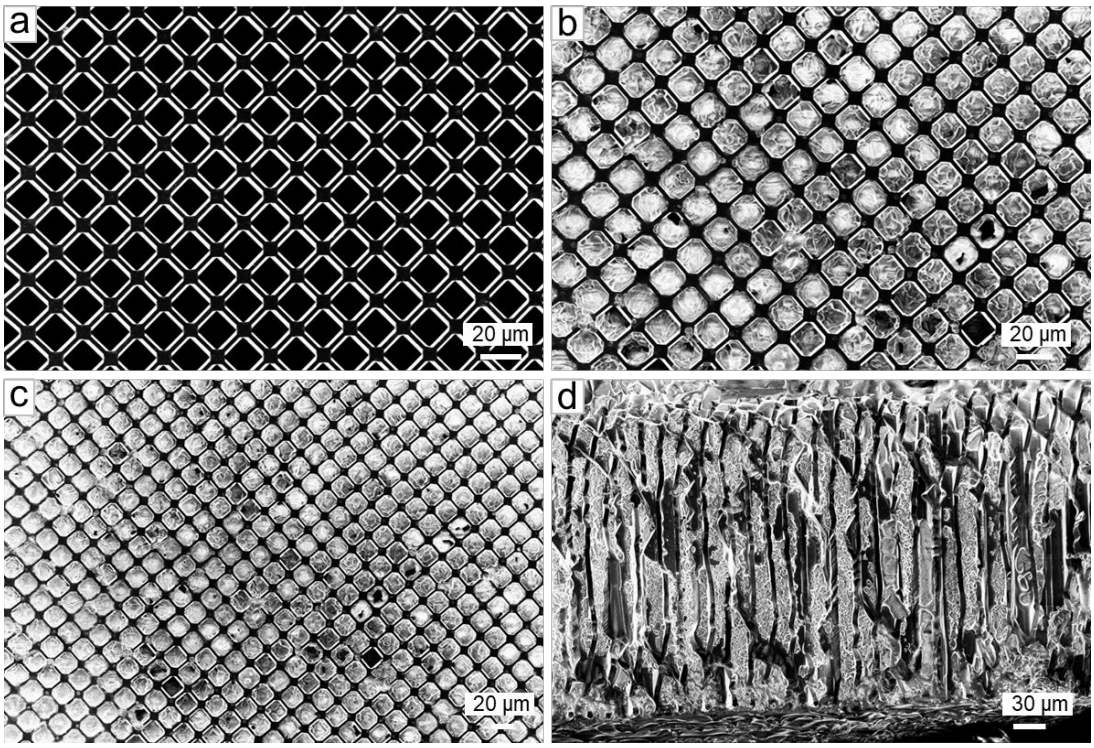

Figure S11. Surface SEM of Si 300 template, b) surface SEM of the CNCI-Si 300 arrays, c) surface SEM of the CNCI-Si 300 arrays, d) cross-sectional SEM image of CNCI-Si 300 arrays.

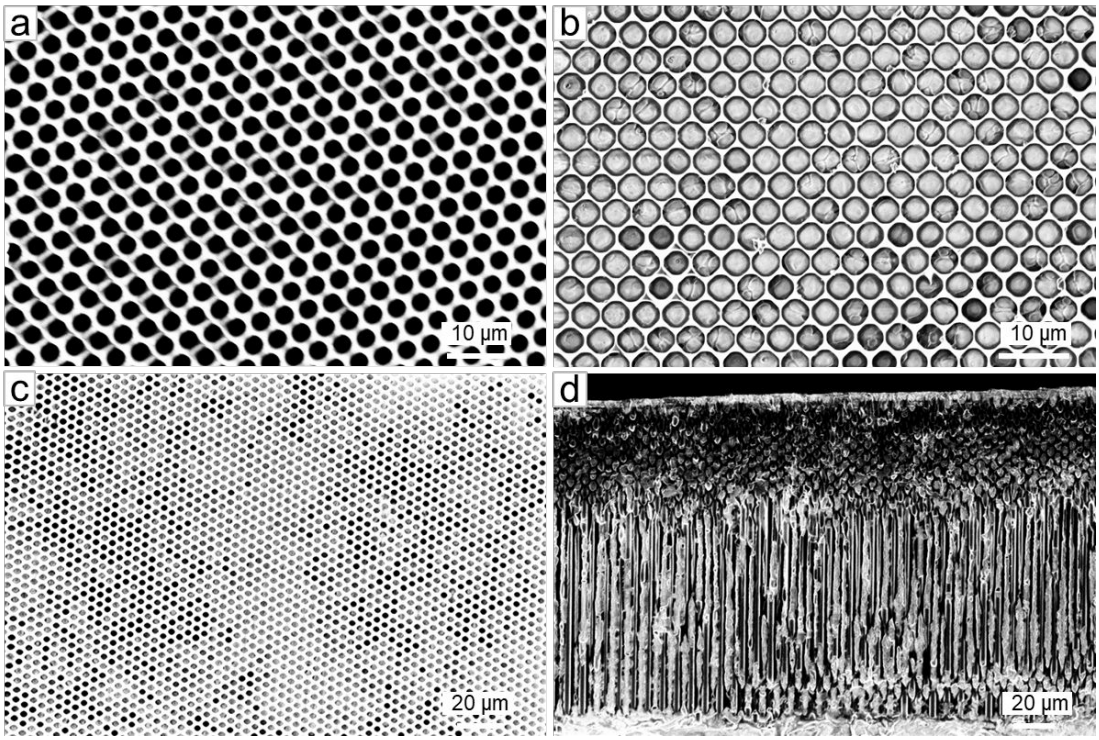

Figure S12. Surface SEM of Si 200 template, b) surface SEM of the CNCI-Si 200 arrays, c) surface SEM of the CNCI-Si 200 arrays, d) cross-sectional SEM image of CNCI-Si 200 arrays.

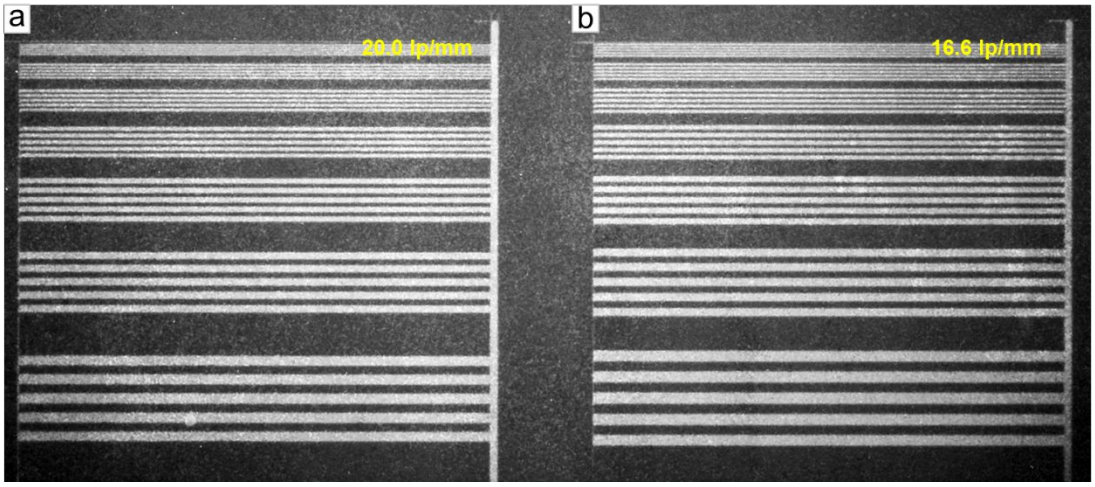

Figure S13. Spatial resolution of the CNCI-Si 400 arrays was determined by a standard line-pair card (lp/mm).

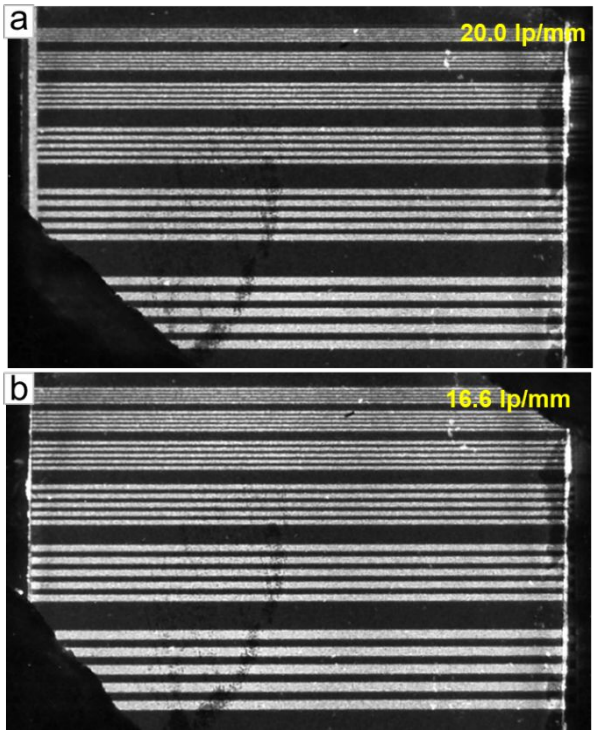

Figure S14. Spatial resolution of the CNCI-Si 300 arrays was determined by a standard line-pair card (lp/mm).

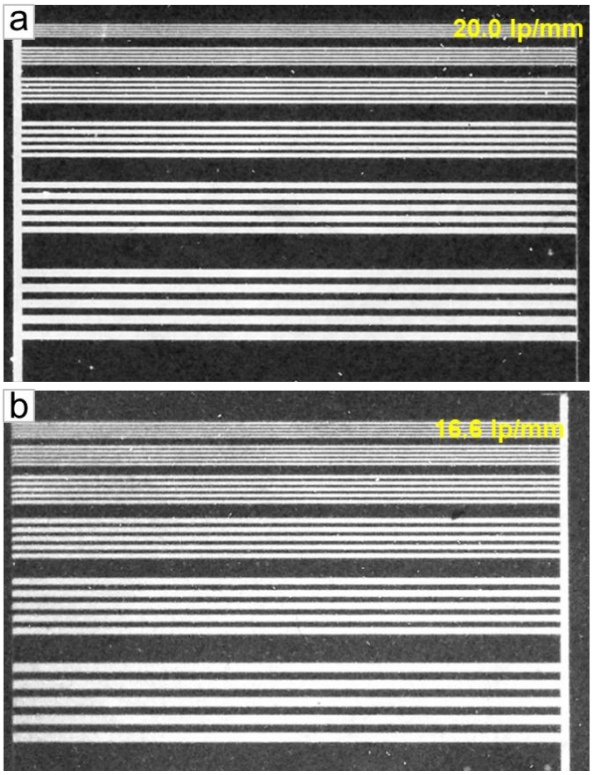

Figure S15. Spatial resolution of the CNCI-Si 200 arrays was determined by a standard line-pair card (lp/mm).

	CNCI-Si 200	CNCI-Si 300	CNCI-Si 400	CNCI-PSF unnormalized	CNCI-PSF normalized
Light output (photons/MeV)	~16 600	~34 100	~43 700	~87 500	~109 000

Table S1. The light output of different CNCI-Si and CNCI-PSF scintillators.

REFERENCES

1. Chen, W.; Zhou, M.; Liu, Y.; Yu, X.; Pi, C.; Yang, Z.; Zhang, H.; Liu, Z.; Wang, T.; Qiu, J.; Yu, S. F.; Yang, Y.; Xu, X. All-Inorganic Perovskite Polymer-Ceramics for Flexible and Refreshable X-Ray Imaging. *Adv. Funct. Mater.* **2021**, *32*, 2107424.